Variance in baroclinic modes across frequency bands in a global ocean simulation with atmospheric and tidal forcing

Maarten C. Buijsman[a], Brian K. Arbic[b], Eric P. Chassignet[c], Luna Hiron[c], Jay F. Shriver[d], Miguel Solano[a], Xiaobiao Xu[c]

[a]*School of Ocean Science and Engineering, University of Southern Mississippi, 1020 Balch Blvd, Stennis Space Center, MS 39529, Mississippi, United States*
[b]*Department of Earth and Environmental Sciences, University of Michigan, 428 Church St, Ann Arbor, MI 48109, Michigan, United States*
[c]*Center for Ocean-Atmospheric Prediction Studies, Florida State University, 2000 Levy Ave 292, Tallahassee, FL 32310, Florida, United States*
[d]*Naval Research Laboratory, 1005 Balch Boulevard, Stennis Space Center, MS 39529, Mississippi, United States*

Abstract

The captured variance, kinetic energy, and energy fluxes for the first ten vertical modes are computed for subtidal, diurnal, semidiurnal, and supertidal frequency bands in a realistically forced global ocean simulation with 41 hybrid vertical coordinates and 1/25° (∼4 km) horizontal grid spacing. In all frequency bands, except the diurnal band, mode 1 constitutes 50-60% of the kinetic energy summed over the first ten modes. The kinetic energy and energy flux in the subtidal eddies in the western boundary and Antarctic Circumpolar currents is predominantly captured by mode 1. In addition to low-mode internal tides, the diurnal band is also affected by near-inertial waves, which enhance the diurnal kinetic energy of the higher modes. The simulation also resolves the first 2-3 propagating supertidal modes. Their mode-1 fluxes are largest near the equator, coinciding with energetic semidiurnal mode-1 waves. The number of modes resolved in the simulation are compared to criteria related to the horizontal and vertical grid spacing. The criterion for the horizontal grid spacing, 6-8 cells per horizontal wavelength, reasonably predicts the resolution of about 4 semidiurnal modes at low latitudes and about 3 supertidal modes globally. The application of a similar criterion, i.e., 6 cells per vertical wavelength, to the isopycnal layers causes an under prediction of the modes resolved. Hence, two newly proposed criteria for the vertical grid spacing are tested.

Keywords: vertical modes, global ocean simulation, energy, tides, resolution
PACS: 92.10.-c, 92.10.Hm, 92.60.Aa
2000 MSC: 74J05, 74J30, 86A05, 76B55

1. Introduction

With the availability of more powerful computing resources, the horizontal and vertical grid spacing of global ocean circulation models that include tidal forcing continuous to increase (Arbic et al., 2018; Arbic, 2022). As a consequence, these models have been able to better resolve the internal wave spectrum (e.g., Simmons et al., 2004; Arbic et al., 2004; Shriver et al., 2012; Muller et al., 2012; Müller et al., 2015; Rocha et al., 2016; Savage et al., 2017; Yu et al., 2019; Li and von Storch, 2020; Buijsman et al., 2020; Arbic et al., 2022; Xu et al., 2022). Realistically forced global ocean circulation models with tides may contribute to numerous topics, e.g., improving our understanding of internal wave driven mixing (Waterhouse et al., 2014; Buijsman et al., 2016), improving the predictability of internal tides (Egbert and Erofeeva, 2021) in the framework of the Surface Water and Ocean Topography (SWOT) mission (Fu et al., 2010; Morrow et al., 2019) and forcing regional circulation models with global internal tides to improve coastal energetics (Siyanbola et al., 2023). In this paper, we evaluate how the horizontal and vertical grid spacing affects the propagation of plane propagating wave modes in subtidal, tidal, and supertidal frequency bands in a global HYbrid Coordinate Ocean Model (HYCOM; Bleck, 2002; Chassignet et al., 2003, 2009) simulation with realistic wind and tidal forcing.

Rossby waves or eddies and internal gravity waves can be decomposed into orthogonal vertical modes, which are a solution of the well-known Stürm-Liouville eigenvalue problem (Gill, 1982). From the local buoyancy frequency, the Stürm-Liouville equation is solved for the eigenfunctions and eigenspeeds. Characteristics of these modes are an increase of the number of zero crossings of the vertical and horizontal velocity eigenfunctions, an increase of the horizontal wavenumber, and a decrease of the eigenspeed for increasing mode number. The solutions of this eigenvalue problem have been used to gain insight into eddies and internal gravity wave propagation. Wunsch (1997) projected vertical modes on subtidally filtered current meter time series of multiple moorings and determined that in most locations the barotropic and first baroclinic modes dominate. Chelton et al. (1998) used the Rossby wave eigenspeeds to map the global distribution of the first baroclinic Rossby radius of deformation. In a global eddy tracking study, Chelton et al. (2011) found that the propagation speeds of the tracked eddies compared well with the theoretical baroclinic Rossby wave phase speeds. In a modeling study of the Agulhas region, Tedesco et al. (2022) projected the velocity and buoyancy eigenfunctions on three-dimensional (3D) model fields to compute eddy and eddy-wave interaction energy terms, following the approach by Kelly and Lermusiaux (2016) and Kelly (2016). In these latter two studies, and many others (e.g., Zilberman et al., 2009; Buijsman et al., 2010; Kelly et al., 2012; Zhao et al., 2016; Buijsman et al., 2020; Gong et al., 2021; Kelly et al., 2021; Pan et al., 2021; Raja et al., 2022), the modal framework has been applied to understand tidal and near-inertial internal gravity wave generation, propagation, and interactions with topography and background flow. While modal energetics in global ocean simulations have been computed for tidal internal waves (internal tides) (e.g., Buijsman et al., 2020; Kelly et al., 2021) and near-inertial waves (e.g., Simmons and Alford, 2012; Raja et al., 2022), the global energetics of subtidal Rossby wave and supertidal internal gravity wave modes in global ocean simulations have not yet been documented.

The number of resolved vertical modes in hydrostatic (global) simulations depends on the vertical and horizontal grid spacing. Following Hallberg (2013), Stewart et al. (2017) diagnose the optimal vertical grid distribution, given a horizontal grid spacing, to represent subtidal baroclinic modal structures in ocean simulations without tidal forcing. They find that for their z-coordinate global ocean model, "at least 50 well-positioned vertical levels are required to resolve the first baroclinic mode, with an additional 25 levels per subsequent mode". Buijsman et al. (2020) compares the energy content of semidiurnal internal tide modes in global HYCOM simulations with a horizontal grid spacing of $1/12.5°$ (8 km) and $1/25°$ (4 km) and 41 hybrid vertical layers. They find that the number of resolved modes doubles from about 2-3 in the $1/12.5°$ simulation to 4-5 in the $1/25°$ simulation. Hence, the criterion that requires a minimum of 50 levels to resolve a mode 1 wave can be considered too strict for the HYCOM simulations, which feature isopycnal layers below the surface mixed layer with z coordinates (see discussion in Xu et al., 2023).

In this paper, we present a global modal decomposition for subtidal, diurnal, semidiurnal, and supertidal frequency bands. We evaluate what modes are resolved as a function of the horizontal and vertical grid spacing, project the modal eigenfunctions on the time varying 3D fields to extract time series of modal amplitudes for velocity and pressure, and compute the captured variance by the modes and their energetics. The research questions that we address in this paper are: 1) what Rossby and internal gravity wave modes are resolved at what frequencies? 2) is the horizontal or vertical grid spacing the limiting factor in resolving these modes? and 3) what is the energy content in these modes?

In the remainder of this paper, in the Methods section, we discuss the global HYCOM simulation, the modal analysis and energetics, and the criteria that govern the resolution of modes. In the Results section, we apply these criteria to the HYCOM simulation, evaluate the variance captured by the modes, and diagnose the modal energetics for the four frequency bands. In the fourth section we discuss our findings. We end with conclusions.

2. Methods

2.1. Model

We use a global HYCOM simulation forced with tides and 3-hourly winds (expt_19.0), which has also been described in Raja et al. (2022). The simulation has 41 hybrid layers and a tripole grid with a horizontal grid spacing of 1/25° (4 km at the equator). The hybrid grid comprises about ∼20 z-coordinate levels covering the surface mixed layer, isopycnal layers in the stratified interior, and terrain-following coordinates on the shelves. The thickness of the z-coordinate layers ranges from 1 m at the surface to 8 m near the bottom of the mixed layer. The depth of the deepest z coordinate varies globally and is about 100-200 m at low to mid latitudes. The model simulation is forced with five tidal constituents, i.e., M_2, S_2, N_2, O_1, and K_1. For the best tidal performance, a spatially varying self attraction and loading term in conjunction with a Kalman filter and a wave drag are applied (Ngodock et al., 2016). The simulation is initialized on 1 April 2019 from a simulation that is constrained by data assimilation (DA). It is run forward for about 50 days to allow transients associated with the DA to dampen out. In this paper, we diagnose hourly 3D output over 30 days from 20 May to 19 June 2019. We perform our diagnostics for every other horizontal grid point to speed up our analyses and limit storage by a factor of four.

An older model simulation for September 2016 (expt_22.0) with the same set-up as expt_19.0 has shown to be in good agreement with M_2 surface and internal tide observations (Buijsman et al., 2020). For an overview of studies that have validated realistically-forced HYCOM simulations with observations over a range of frequencies, we refer to Arbic (2022).

2.2. Modal Energetics

We solve the hydrostatic Stürm-Liouville eigenvalue problem

$$\frac{\partial^2 \mathcal{W}_n}{\partial z^2} + \frac{N^2}{c_n^2}\mathcal{W}_n = 0 \tag{1}$$

for the first 10 modes for a 30-day time-mean and spatially varying buoyancy frequency $N(z)$, where $\mathcal{W}_n$ is the vertical velocity eigenfunction of mode n, c_n is the eigenspeed, and z is the vertical coordinate. Next, we project the normalized horizontal velocity eigenfunctions $\mathcal{U}_n = \partial \mathcal{W}_n/\partial z$ on the 3D hourly time series of the HYCOM simulation to compute the modal amplitudes of the horizontal baroclinic velocities and perturbation pressures at each horizontal coordinate

$$\begin{aligned} \mathbf{u}(z,t) &= \Sigma_n \hat{\mathbf{u}}_n(t)\mathcal{U}_n(z), \\ p(z,t) &= \Sigma_n \hat{p}_n(t)\mathcal{U}_n(z), \end{aligned} \tag{2}$$

where $\mathbf{u} = (u, v)$ is the horizontal baroclinic velocity vector with velocities u and v along the x and y coordinates, respectively, p is the perturbation pressure, and $\hat{\mathbf{u}}_n$ and $\hat{p}_n$ are the modal amplitudes for velocity and pressure, respectively. For further details on these calculations, the reader is referred to Buijsman et al. (2020) and Raja et al. (2022).

While Raja et al. (2022) only diagnosed the near-inertial band motions in twin simulations with (expt_19.0) and without (expt_19.2) tides, in this paper we consider the modal dynamics across all tidal and non-tidal frequency bands in a spectral analysis. First, we apply a Tukey window with cosine fraction $\alpha = 0.2$ to the modal amplitude time series of velocity and perturbation pressures to minimize spectral leakage. We find that for $\alpha = 0.2$ the time-series variance is reduced by 7%. The results for $\alpha = 0.5$ are visually similar, while the variance is further reduced by 17%. We confirm that when the Tukey window is not applied, the spurious energy in the supertidal band is large at locations where subtidal energy is large, e.g., the Antarctic Circumpolar Current (ACC).

In a next step, we Fast Fourier Transform the modal amplitude time series. For each frequency and mode number, we compute time-mean modal

Kinetic Energy (KE_n) and the horizontal pressure flux vector $\mathbf{F}_n$ using the Fourier coefficients as in Kelly et al. (2012). Finally, we integrate the energy terms over four frequency bands: (1) subtidal, 0.0333-0.85 cycles per day (cpd), (2) diurnal (D1), 0.85-1.05 cpd, (3) semidiurnal (D2), 1.78-2.15 cpd, and (4) higher harmonic (HH; supertidal), 2.15-12 cpd. The near-inertial band is excluded from this analysis because it is extensively discussed in Raja et al. (2022). We note that the diurnal and subtidal bands equatorward of $\pm 30°$ latitude are impacted by near-inertial waves.

2.3. Criteria to Determine the Number of Resolved Modes

In this section, we explain the methods that determine how many (sub)tidal modes are resolved by the horizontal and vertical grid spacing of our global HYCOM simulation. We follow the approach by Hallberg (2013) and Stewart et al. (2017), who evaluated the resolution requirements for subtidal modes in global simulations. We use the term "subtidal" to also imply "subinertial".

First, we evaluate the effect of the horizontal grid spacing. Subtidal modes have wavelengths (Stewart et al., 2017)

$$\lambda_{\mathrm{s},n} = 2\pi \sqrt{\frac{c_n^2}{f^2 + 2\beta c_n}}, \tag{3}$$

where subscript s refers to subtidal, c_n is the eigenspeed, f is the inertial frequency, β is the meridional gradient of f, and the square-root-term is the mode-n baroclinic deformation radius. The wavelengths of internal wave modes are computed as

$$\lambda_{\omega,n} = 2\pi \frac{c_n}{\sqrt{\omega^2 - f^2}}, \tag{4}$$

where ω is the internal wave frequency.

Because the horizontal grid spacings $(\Delta x, \Delta y)$ vary on the HYCOM tripole grid, it is convenient to represent the model horizontal resolution by the effective horizontal grid spacing (Hallberg, 2013; Stewart et al., 2017)

$$\tilde{\Delta} = \sqrt{\frac{\Delta x^2 + \Delta y^2}{2}}. \tag{5}$$

To resolve the horizontal wavelengths of (sub)tidal modes, the effective horizontal grid spacing needs to be

$$\tilde{\Delta} \leq \frac{\lambda_n}{\gamma}, \tag{6}$$

where γ is the number of gridcells per wavelength, which should be larger than 2π (Hallberg, 2013). In Appendix A, we consider how finite difference errors of a sinusoidal wave change as a function of the horizontal grid spacing. We compute amplitude errors of $17-10\%$ for 6-8 grid cells per wavelength. We use this range to evaluate the number of modes resolved for the subtidal and the K_1, M_2, and M_4 frequencies. We select these tidal constituents because they are the dominant frequencies in the D1, D2, and HH frequency bands, respectively (see also the discussion of Figure 10).

Stewart et al. (2017) applies a similar criterion to determine what modes are resolved for a vertical z grid. They state that "having at least six points per wavelength permits interpolation between points to locate peaks, troughs, and zero crossings"; i.e., the vertical grid is required to have at least three grid points between subsequent modal zero crossings $z_{\mathcal{U}0}$ of the horizontal velocity eigenfunction. This criterion, referred to as CZ1, is formulated as

$$\Delta z \leq \frac{\Delta z_{\mathcal{U}0}}{3}, \tag{7}$$

where Δz is the time-mean and vertical layer thickness of the z grid and $\Delta z_{\mathcal{U}0}$ is the vertical distance between zero crossings. Based on this and some other criteria, Stewart et al. (2017) recommends that a z-coordinate model requires about 50 levels to accurately resolve mode 1, and an additional 25 to resolve each subsequent mode. Our HYCOM simulation uses a maximum of 41 hybrid layers, but in most of the stratified interior fewer layers are used. Clearly, the resolution of propagating modes requires fewer levels in isopyncal models than in z-level models, as has been shown in Buijsman et al. (2020) and Xu et al. (2023).

HYCOM's hybrid vertical coordinate has z levels in the mixed layer and isopycnal layers below that. While we can apply criterion CZ1 to the surface layers, we may need to use a different criterion for the isopycnal layers. One could argue that, in order to resolve a certain mode number in an isopycnal model, all $\mathcal{U}$ zero-crossings of that mode should coincide with the layer interfaces (Xu et al., 2023), such that the maximum horizontal velocity amplitudes occur inside the layers. As a consequence of this choice, all $\mathcal{W}$ zero-crossings should occur inside the layers and the maximum vertical velocity amplitudes at the layer interfaces. However, the layer positioning in HYCOM has not been designed with the aim of resolving a certain high vertical mode number. In addition to CZ1, we apply two additional criteria, which are relatively crude, to evaluate how many Rossby and internal wave modes are resolved by the vertical grid in HYCOM. In the second criterion, CZ2, we argue that a mode is not resolved when one $\mathcal{U}$ and one $\mathcal{W}$ zero-crossing occur in the same layer. In the third criterion, CZ3, we argue that a mode is not resolved if a layer contains either two $\mathcal{U}$ or two $\mathcal{W}$ zero-crossings. As we will demonstrate later, the application of CZ1 to the z levels of the hybrid vertical coordinate grid allows for the resolution of much higher mode numbers than the application of either CZ2 or CZ3 to the isopycnal layers. We provide an overview of all criteria in Table 1, which the reader can use as a reference in the Results and Discussion sections.

Table 1: Criteria that determine when a vertical mode is not resolved by the horizontal or vertical grid spacing.

horizontal grid spacing		fewer than 6-8 cells per wavelength
vertical grid spacing	CZ1	fewer than 3 z levels between subsequent $\mathcal{U}$ zero crossings
	CZ2	one $\mathcal{U}$ and one $\mathcal{W}$ zero-crossing occur in the same isopycnal layer
	CZ3	either two $\mathcal{U}$ or two $\mathcal{W}$ zero-crossings occur in the same isopycnal layer

To minimize errors in the locations of the zero crossings and eigenspeeds due to the thicker deeper layers in HYCOM, we first interpolate the $N(z)$ profiles to a vertical grid that adopts the existing fixed z layers with $\Delta z < 20$ m near the surface and an equidistant $\Delta z \approx 20$ m below. We solve for 20 eigenmodes at every second grid point in the x and y directions to reduce computation time. We then linearly interpolate to find the vertical positions where $\mathcal{W} = 0$ and $\mathcal{U} = 0$. This vertical grid is only used to more accurately determine the locations of the zero crossings and eigenspeeds. This method is not used for the variance and energy term calculations, which are done on the native 41-layer grid.

3. Results

3.1. Eigenfunctions

The normalized horizontal velocity eigenfunctions for the first five modes near the Kuroshio, in the equatorial Pacific, and in the Southern Ocean display some spatial variability in Figure 1. The equatorial Pacific features

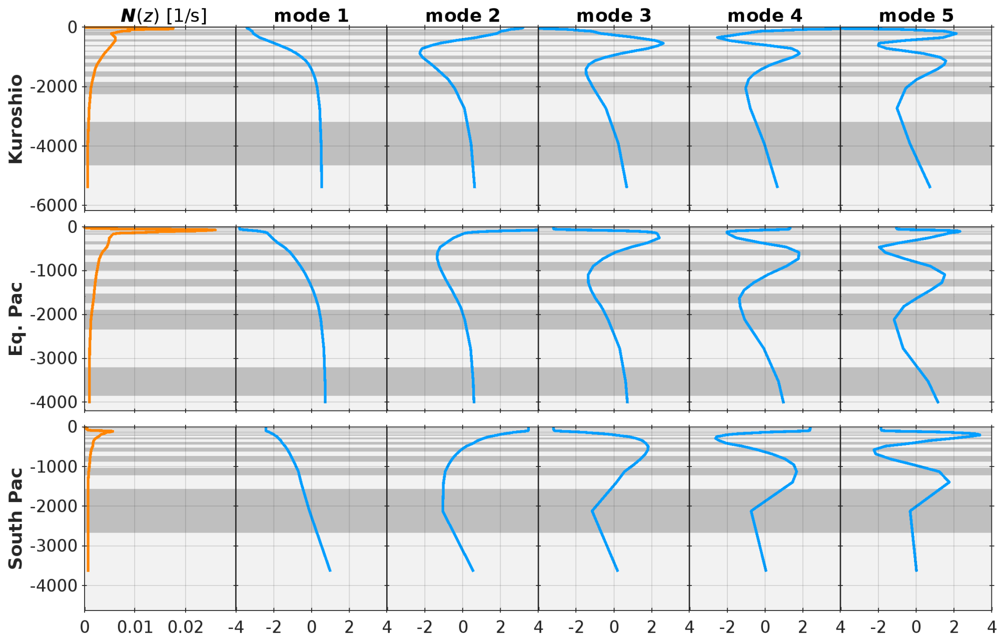

Figure 1: The buoyancy frequencies (first column) and the first five $\mathcal{U}$ eigenfunctions computed at three locations in the Pacific Ocean: a mid-latitude location (Kuroshio at 27.98°N and 150°E; top), the equator (Eq.Pac at 2.84°S and 228°E; middle), and the Southern Ocean (South Pac. at 66.85°S and 228°E; bottom). The time-mean layer thicknesses are alternately shaded with dark and light gray colors. The $\mathcal{U}$ eigenfunctions are unitless.

the strongest surface intensified buoyancy frequency $N(z)$ and a more equal distribution of layer thicknesses in the deep ocean. Because of this relatively equal distribution, the higher modes are better resolved at depth, e.g., the curvature is realistic and the amplitudes between the zero-crossing are captured. In contrast, at the mid and higher latitudes the layer thickness distribution becomes more skewed with larger layer thicknesses at depth. This causes higher modes to be less well resolved (e.g., modes 2-5 in the South Pacific in Figure 1).

3.2. Resolved Modes

The mode-1 wavelengths (eqs. 3 and 4) and the number of resolved subtidal, K_1, M_2, and M_4 modes due to the horizontal grid spacing (eq. 6) are shown in Figures 2 and 3a-d. The zonal mean of the number of the resolved modes for seafloor depths > 2000 m and averaged over 10° latitude bins is presented in Figure 4. In accordance with the poleward decrease of the

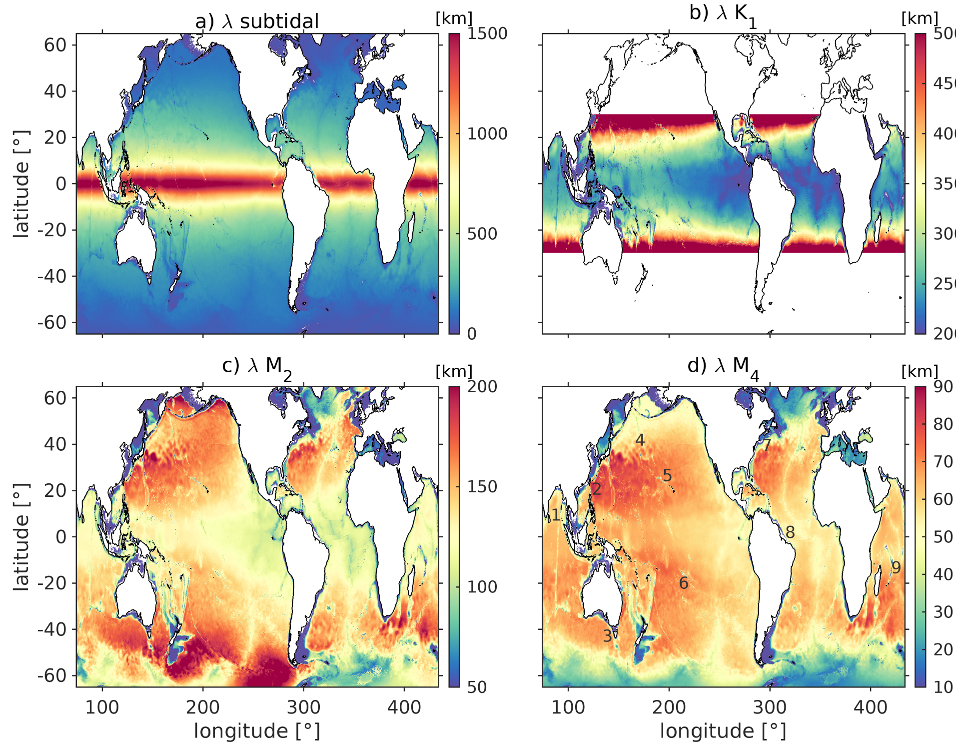

Figure 2: The mode-1 wavelengths for (a) the subtidal mode and the (b) K_1, (c) M_2, and (d) M_4 internal tides. All colorbars have different scales. The numbers in (d) refer to the following geographic locations: 1) Bay of Bengal, 2) Luzon Strait, 3) Tasmania, 4) Emperor Seamounts, 5) Hawaii, 6) French Polynesian Islands, 7) Georges Bank, 8) Amazon Shelf, and 9) Mascarene Ridge.

subtidal wavelength in Figure 2a (see also Chelton et al., 1998), the number of resolved subtidal modes rapidly decreases poleward (Figures 3a and 4a). The meridional trends of the wavelengths and the number of modes resolved for the internal tides are opposite to those of the subtidal modes. Internal wave modes with lower frequencies have longer wavelengths (Figure 2b-d), and hence, they are better resolved by the horizontal grid spacing, which also decreases poleward. For the diurnal K_1 internal tide (Figure 4b), on average eight modes are resolved at the equator and the number increases towards 20 modes near the K_1 turning latitude due to the increase in wavelength. The shorter wavelength M_2 internal tide has fewer modes resolved, with a

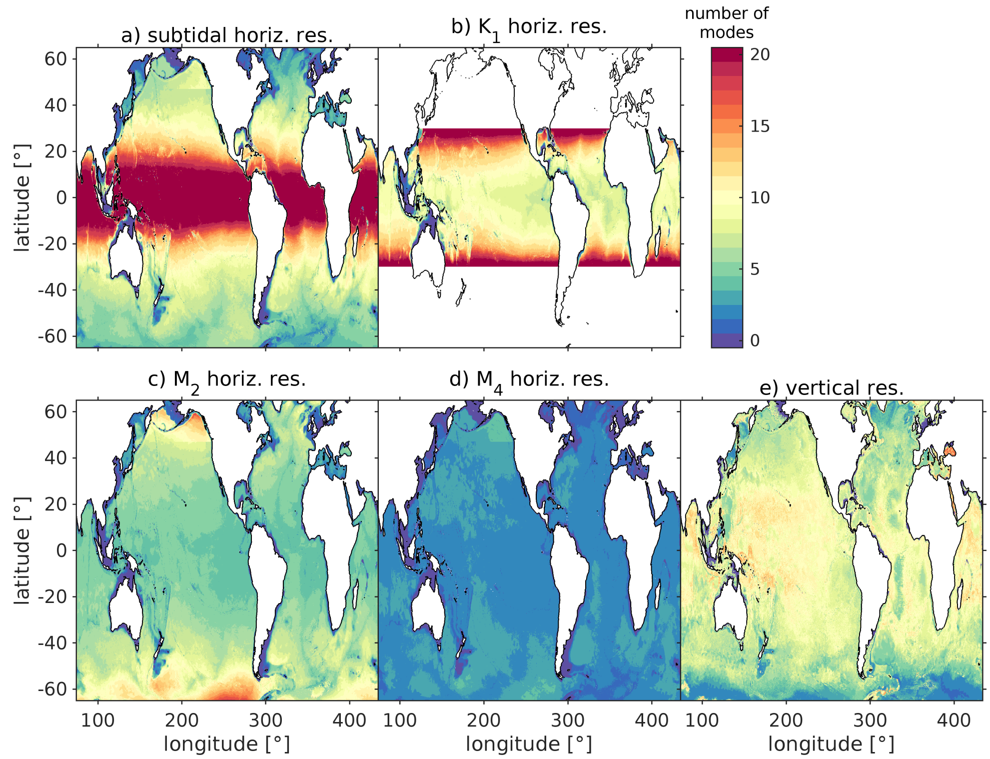

Figure 3: The number of resolved modes, limited to 20, depending on the horizontal grid spacing for (a) the subtidal modes and the (b) K_1, (c) M_2, and (d) M_4 internal tides. The subplots show the mean value of the number of resolved modes computed for $\gamma = 6$ and 8. (e) The number of resolved modes depending on the vertical grid spacing according to criterion CZ3.

minimum number of about 4 modes at the equator (Figure 4c). Due to the large zonal variability in the M_2 wavelength poleward of $\sim 40°$ (Figure 2c), the standard deviation in the number of resolved modes due to the horizontal grid spacing increases significantly in Figure 4c. On average, only the first two M_4 modes are resolved (Figure 4d). In contrast to the (semi)diurnal tides, the number of resolved M_4 modes remains constant equatorward of $\pm 50°$ because the poleward increase in the mode 1 and 2 wavelengths is much smaller than for the K_1 and M_2 internal tides (Figure 2c and d). Poleward of $\pm 50°$, the smaller horizontal grid sizes of the tripole grid compensate somewhat for the decrease in wavelength.

In contrast to the horizontal grid spacing, the number of resolved modes in Figure 4 is more sensitive to the different vertical grid-spacing criteria (Table 1). If CZ1 is applied to the hybrid vertical coordinate over the full water column (referred to as CZ1-h in Figure 4), mode 1 is barely resolved at the low latitudes and not at all in the southern oceans. On the other hand, if CZ1 is only applied to the z levels (referred to as CZ1-z in Figure 4), more than 8 modes are resolved. Clearly, CZ1 limits the number of modes resolved when it is applied to isopycnal coordinates, which feature thicker layers in the deep ocean (Figure 1). Criteria CZ2 and CZ3 have similar meridional trends and allow for the resolution of more modes than CZ1-h (Figure 4). They predict that on average 6 and 12 modes are resolved in the tropics, respectively, and the number of resolved modes decreases poleward due to the reduction in stratification and the increase in layer thicknesses in the deep ocean. Because the vertical distance between subsequent $\mathcal{U}$ and $\mathcal{W}$ zero crossings is smaller than the distance between pairs of subsequent $\mathcal{U}$ zero crossings or pairs of subsequent $\mathcal{W}$ zero crossings, CZ2 is more strict than CZ3. For tidal modes, the number of resolved modes as a function of latitude due to CZ2 and CZ3 in Figure 4 has opposite trends than the number of resolved modes due the horizontal grid spacing. This suggests that for the dominant M_2 internal tides the horizontal grid spacing is the limiting factor at low latitudes, while the vertical grid spacing is the limiting factor at higher latitudes. In the Discussion section, we will compare the variance in the simulated modes (discussed next) to these "predictions" and evaluate which of the vertical grid spacing criteria is the most suitable.

3.3. Captured Variance

Next, we compute how much of the total variance in baroclinic velocities and pressures is captured by the modes for the four frequency bands. The depth-averaged variance captured by the sum of modes 1 to n is expressed as the coefficient of determination (Emery and Thomson, 2001)

$$R_n^2 = \frac{1}{H^*} \int 1 - \frac{SS_{\mathrm{res},n}}{SS_{\mathrm{tot}}} dz^*, \tag{8}$$

where $SS_{\mathrm{res},n}$ is the variance of the difference between the fit of the sum of modes 1 to n and the undecomposed time series of baroclinic velocities or pressures for each layer, SS_{tot} is the variance of the undecomposed time series for each layer, and H^* and z^* are the Wentzel-Kramer-Brillouin (WKB)

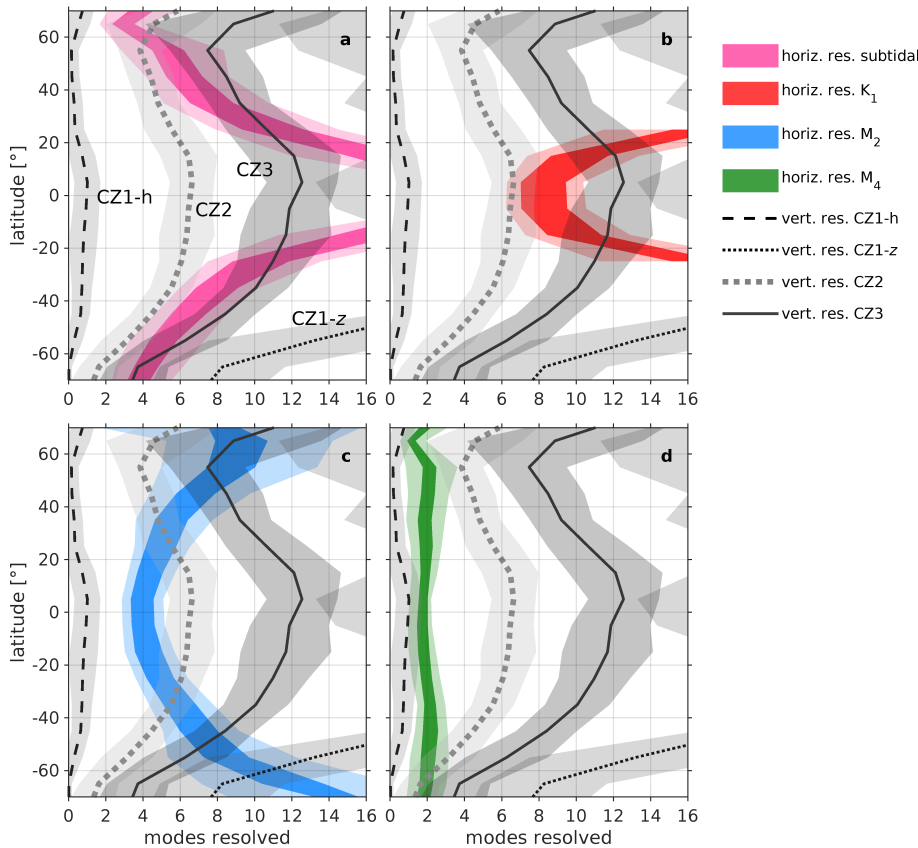

Figure 4: The number of modes resolved for the horizontal and the vertical grid spacing area-averaged over longitude and 10° latitude bins. The colored polygons indicate the number of resolved (a) subtidal, (b) K_1, (c) M_2, and (d) M_4 modes due to the horizontal grid spacing. The dark-colored polygons mark the extent of the zonal-mean values for $\gamma = 6$ and 8 and the light-colored polygons mark the extent of the zonal-mean values $\pm$ one standard deviation. The gray and black (dashed) lines mark the zonal-average for the vertical grid-spacing criteria CZ1-3. The gray shaded polygons mark the extent of the zonal-mean values $\pm$ one standard deviation. These lines and gray polygons are identical in (a-d). In CZ1-h, the Stewart et al. (2017) criterion is applied to the hybrid coordinates, whereas in CZ1-z, it is applied to the z coordinates of the mixed layer.

stretched (Althaus et al., 2003) water depth and vertical coordinate, respectively. $SS_{\mathrm{res},n}$ and SS_{tot} are based on the power spectral densities of the

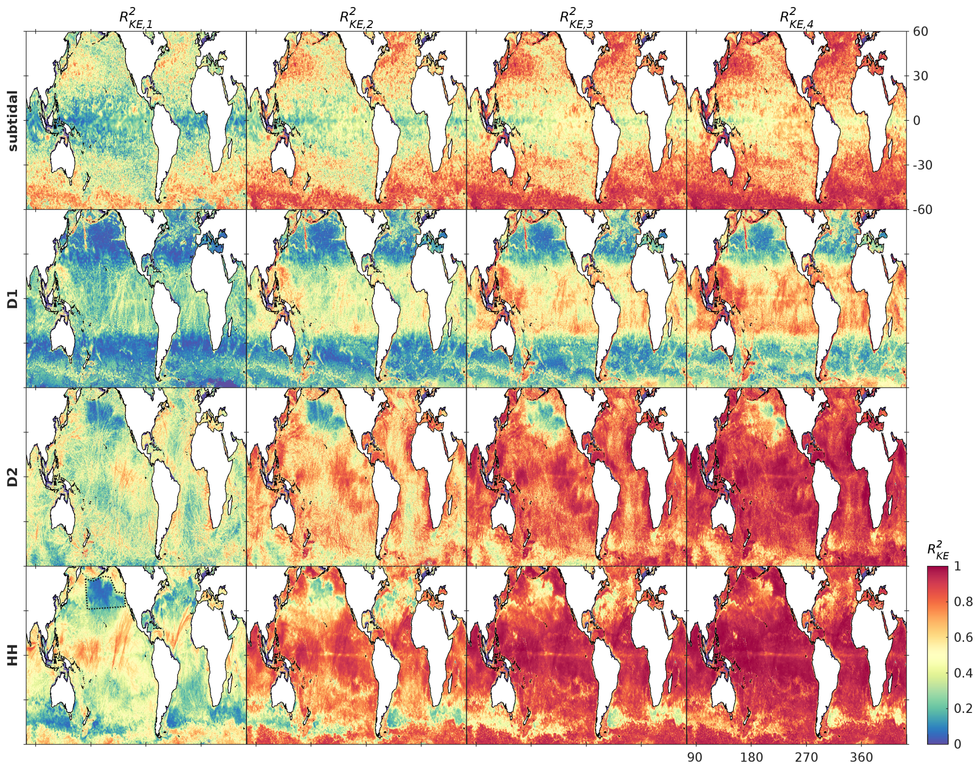

Figure 5: The captured variance $R^2_{KE,n}$ of the baroclinic velocities summed over modes 1 to n for the first four modes for the four frequency bands. The dotted dark gray polygon in the bottom left subplot marks the area in the North Pacific affected by thermobaric instabilities.

difference and undecomposed time series, respectively. The velocity variance is computed by summing over the x and y velocity variances. The coefficient of determination for each layer is vertically averaged over the time-mean layer thicknesses that are WKB stretched. This is done to increase the relative importance of the surface layers, where the velocities and perturbation pressures are largest.

The spatial maps of the captured velocity variance, $R^2_{KE,n}$, up to mode 4 in Figure 5 and its zonal average over 10° latitude bins up to mode 10 in Figure 6a-d portray large variability in space and per frequency band. Spatial maps of $R^2_{KE,n}$ for $n > 4$ are not shown because they do not add additional insight. Mode one generally captures most of the variance in all frequency bands.

The subtidal velocity variance of eddies in the Antarctic Circumpolar and the western boundary currents project on the gravest modes (top row of Figure 5 and Figure 6a). In contrast, higher modes become relatively more important at lower latitudes (Figure 6a).

The diurnal variance captured by the modes is large equatorward of the diurnal turning latitudes and largest in the western Pacific (second row of Figure 5 and Figure 6b). Poleward of these turning latitudes, the captured velocity variance is relatively large near underwater topography, where diurnal tides are trapped (e.g., the Emperor Seamounts at 42.7°N and 170.4°E in the northwest Pacific Ocean; their geographic location and other locations mentioned in the text are shown in Figure 2d). Variance in mesoscale eddies in the ACC is also captured by diurnal modes.

In contrast to the diurnal variance, the semidiurnal velocity variance is generally equally distributed across the ocean and projects on fewer modes (modes 4-5; third row of Figure 5 and Figure 6c).

Equatorward of ±20°, supertidal modes 3-4 capture most of the variance (fourth row of Figure 5 and Figure 6d). Specifically, the captured mode-1 variance is large in the Bay of Bengal, the western Pacific, to the north of the French Polynesian Islands (18.1°S and 217.7°E), the Amazon Shelf (2.2°N and 312.5°E), and northeast of Madagascar, including the Mascarene Ridge (12.6°S and 60.9°E). We will later show that strong semidiurnal internal tides evolve into nonlinear supertidal waves in these areas. At higher latitudes, supertidal variance also projects on higher modes, which is most likely associated with mesoscale eddies.

The lower semidiurnal and supertidal $R^2_{KE,n}$ in the north Pacific Ocean (Figure 5) is due to numerical noise that project on higher semidiurnal modes and all supertidal modes. This noise is most likely associated with thermobaric instabilities (TBI; Buijsman et al., 2016, 2020; Raja et al., 2022).

The captured pressure variance $R^2_{p,n}$ is only presented in Figure 6e-h as a zonal average. For the sake of brevity, we do not show spatial maps of $R^2_{p,n}$. In contrast to the captured velocity variance in Figure 6a-d, the captured pressure variance features more variance in mode 1, less variance in the higher modes, and the captured variance approaches unity in all frequency bands, i.e, all the variance is explained by the modes. While the meridional trends in the captured mode 1 velocity and pressure variance are somewhat similar, the trends are more muted for the pressure variance.

The difference in the captured variance between the velocity and pressure modes may be attributed to several reasons. The vertical baroclinic velocity profiles are generally "noisier" than the perturbation pressure profiles. This "noise" may project on higher velocity modes. The pressure profiles are smoother because they are based on vertically integrated perturbation densities. Moreover, near-inertial wave and possibly subtidal motions may feature strong horizontal velocities that project on higher modes, but they lack (strong) vertical motions. Hence, these standing-wave features contribute little to the high-mode pressure variance. In the Discussion section we show that this difference affects the interpretation of the predictability of the horizontal and vertical grid-spacing criteria.

3.4. Energetics

3.4.1. Global Patterns

We compute the time-mean and depth-integrated modal kinetic energy and pressure fluxes for the four frequency bands and present them in Figures 7 and 8 for the first four modes. The spatial patterns for KE_n and $|\mathbf{F}_n|$ are similar, although some subtle differences exist. For diurnal modes near the diurnal turning latitudes ($\pm 30°$), near-inertial motions due to wind (e.g., Raja et al., 2022) and parametric subharmonic instabilities (PSI; e.g., Hazewinkel and Winters, 2011; Ansong et al., 2018) significantly enhance the kinetic energy of the higher modes (Figure 7), whereas the energy fluxes of the higher modes are much smaller as compared to mode 1 (Figure 8). The latter is attributed to the reduced high-mode variance in the diurnal perturbation pressures (Figure 6f). Both the KE and energy flux of the semidiurnal modes 3 and higher and all supertidal modes are elevated due to the aforementioned TBI in the northeastern Pacific Ocean.

A new result of this paper is the global decomposition of modes in the subtidal and supertidal frequency bands. The magnitude of the subtidal mode 1 pressure fluxes is $> 10^4$ W/m and these large fluxes mostly occur in the western boundary current and ACC eddies (top row of Figure 8). In the next section we will present some regional characteristics of these fluxes.

The strongest diurnal fluxes with magnitudes of $\mathcal{O}(10^4)$ W/m radiate southeastward from Luzon Strait (20.5°N and 121.4°E; second row of Figure 8). Smaller diurnal mode 1 fluxes of $\mathcal{O}(10^2)$ W/m appear to radiate equatorward from the diurnal turning latitudes near $\pm 30°$ (Figure 8). Although some of these fluxes are from tidal origin, they can also be due to wind-generated near-inertial internal waves.

In contrast to the diurnal energy flux, the semidiurnal energy flux is more equally distributed over the global ocean (third row of Figure 8). These fluxes

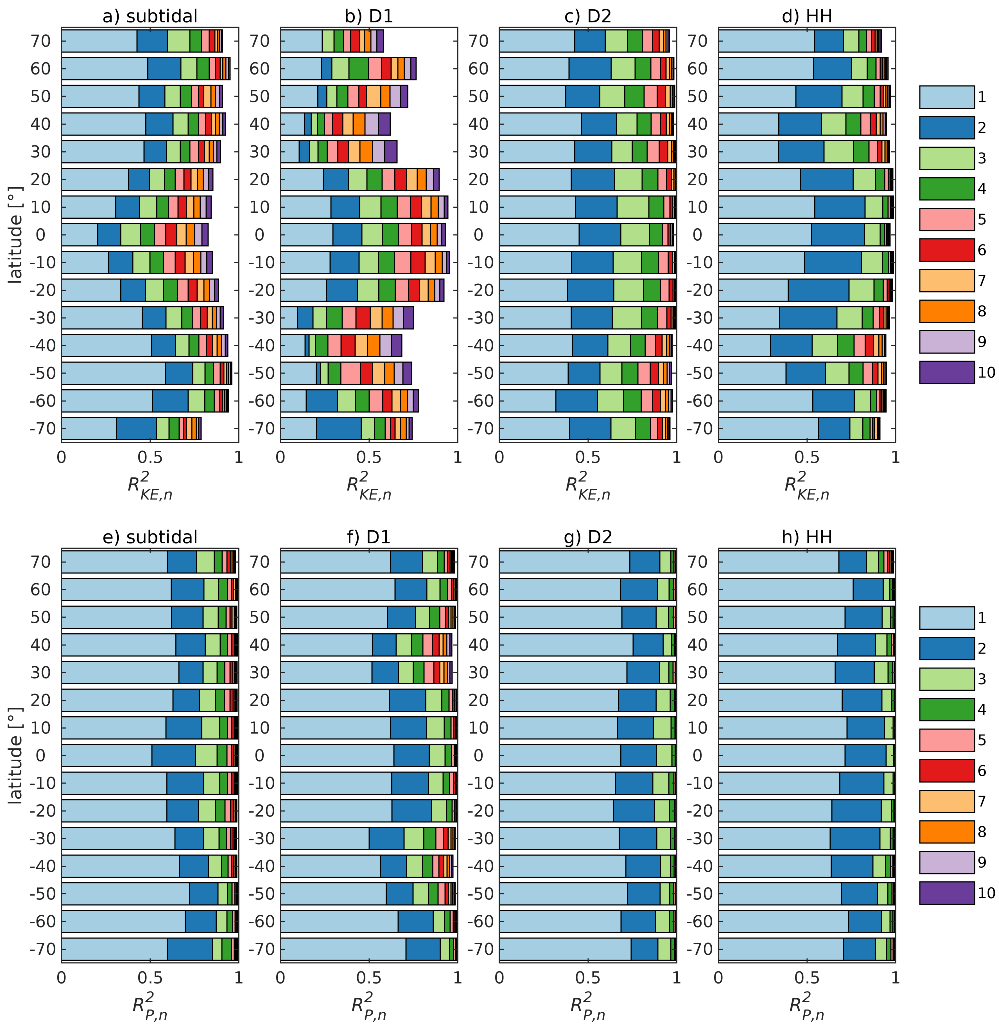

Figure 6: Stacked bargraph of zonally area-averaged captured velocity variance $R^2_{KE,n}$ for the first 10 modes for the (a) subtidal, (b) diurnal, (c) semidiurnal, and (d) supertidal frequency bands. The captured pressure variance $R^2_{p,n}$ is in (e-h). R^2_n is zonally averaged over 10° latitude bins for seafloor depths > 2000 m. Each colored rectangle represents the increase in R^2_n for each additional mode n. R^2_n inside the TBI area (Figure 5) is excluded for all semidiurnal and supertidal modes.

are mostly attributed to the M_2 internal tide, which has been extensively discussed and validated in Buijsman et al. (2020). Moreover, semidiurnal high-mode fluxes are larger and more widespread than the diurnal high-mode

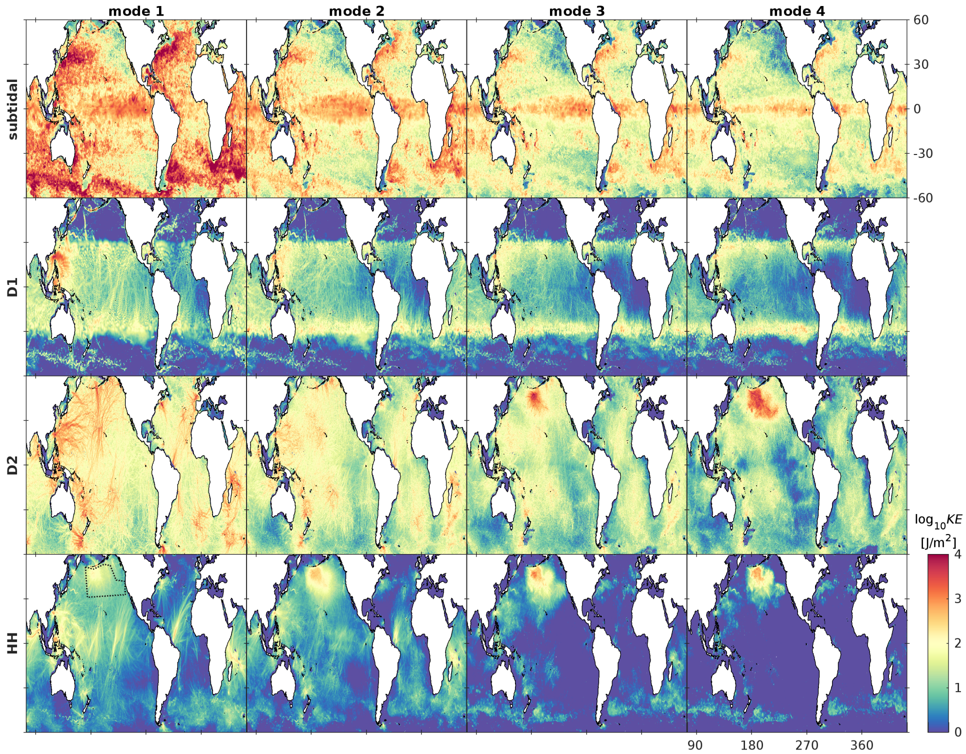

Figure 7: The time-mean and depth-integrated kinetic energy for modes 1 to 4 and the four frequency bands. The dotted dark gray polygon in the bottom left subplot marks the extent of the thermobaric instabilities.

fluxes. This may be because strong diurnal internal tides are only generated in the northwest Pacific Ocean.

Supertidal fluxes in the bottom row of Figure 8 are largest for modes 1 and 2. The strongest supertidal fluxes of $\mathcal{O}(10^3)$ W/m occur near the equator in the Bay of Bengal, near Luzon Strait, offshore of the Amazon Shelf, and near the Mascarene Ridge. These supertidal beams coincide with strong semidurnal internal tide beams (third row of Figure 8).

3.4.2. Zonal Averages and Global Integrals

We area-average the depth-integrated KE zonally over 10° latitude bins for seafloor depths > 2000 m (Figure 9). The subtidal KE is the largest of all frequency bands with energy densities ranging between 5 and 10 kJ/m^2. The subtidal KE is dominated by mode 1, which is the largest at ±40° due to the

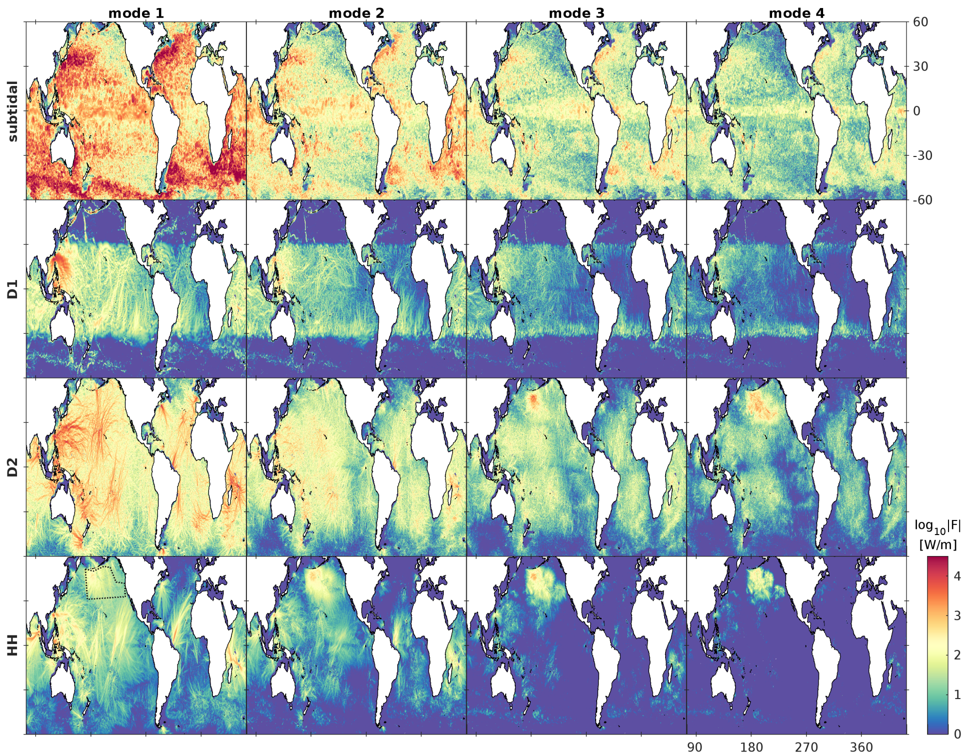

Figure 8: The same as Figure 7, but for the pressure flux magnitude.

eddies in the western boundary currents and the ACC (Figure 9a). Near the equator, the equatorial dynamics also project on higher subtidal modes (see also top row of Figure 7). Diurnal internal tides, with relatively more energy in mode 1, are dominant equatorward of $\pm 30°$, with the largest energy density of $\sim$1 kJ/m^2 at Luzon Strait near 20°N. In contrast, near-inertial motions project on diurnal modes near the turning latitudes (Figure 9b), causing a more equal energy distribution over all modes (Raja et al., 2022). In accordance with Buijsman et al. (2020), the semidiurnal modal kinetic energy in Figure 9c is mostly tidal, dominated by mode 1, and more uniformly distributed with KE densities of 1-2 kJ/m^2. The modal distribution of the supertidal energy reveals two patterns. Equatorward of 15°S-25°N, the energy density for the first ten modes averages 0.15 kJ/m^2 and is dominated by mode 1. Poleward of 15°S and 25°N, the energy density is smaller and mode 1 comprises a smaller fraction of the total KE.

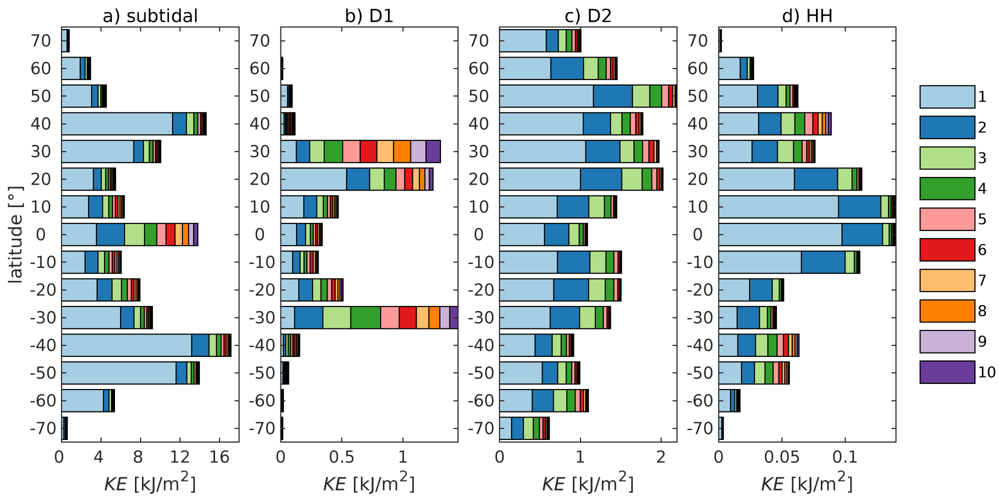

Figure 9: Stacked bargraph of zonally area-averaged modal kinetic energy for modes 1-5 for the (a) subtidal, (b) diurnal, (c) semidiurnal, and (d) supertidal frequency bands. KE is zonally averaged over 10° latitude bins for seafloor depths > 2000 m. The area with TBI has been excluded from the averages for the semidiurnal modes 3-5 and all supertidal modes.

The global integrals of modal KE for seafloor depths > 250 m are listed in Table 2. These values are less than 10% larger than the values for seafloor depths > 2000. We use a cutoff value of 250 m to facilitate comparison with the literature. We multiply the area-integrated values by four to correct for the subsampling. Note that these magnitudes are slightly affected by the Tukey window, which reduces the variance of each modal time series by 7%. Mode 1 comprises 50-62% of the KE summed over ten modes for all bands except for the diurnal band. The subtidal band has the largest amount of KE summed over 10 modes, i.e., 740 PJ, which is more than six times the energy in the semidiurnal band. Using Simple Ocean Data Assimilation (SODA) data (Carton and Giese, 2008), Huang (2010) estimates that the oceans contain about 1460 PJ of Eddy Kinetic Energy, most of which is in eddies. If one assumes that half this energy is associated with baroclinic motions (Ferrari and Wunsch, 2010; Xu et al., 2011), then our value is very close to this estimate. Using a 1/12° global model simulation, Mak et al. (2022) computes an eddy energy of about 9520 PJ. Assuming half of this value is barotropic eddy energy and half of that is baroclinic kinetic energy (Xu et al., 2011), we get about 2400 PJ, which is more than 3 times larger than

Table 2: Global integral of KE per frequency band and modes 1-5 in PJ ($= 10^{15}$ J) for seafloor depths > 250 m. The second column has the latitude range used for the global integral. Modal energy as a fraction of the energy summed over 10 modes (third column) is listed between parentheses in %. The area with TBI has been excluded from the integrals for the semidiurnal modes 3-5 and all supertidal modes. These values are smaller because of the Tukey window. They are extrapolated in space because we only store every other grid cell.

band	lat. range [°]	Σ_1^{10}	1	2	3	4	5
subtidal	-90.0 to 90.0	740.0	446.5 (60)	107.4 (15)	57.8 (8)	35.8 (5)	24.9 (3)
D1	-30.0 to 30.0	34.4	9.5 (28)	6.0 (17)	4.1 (12)	3.5 (10)	2.7 (8)
D2	-74.5 to 74.5	115.4	57.9 (50)	28.8 (25)	13.4 (12)	6.9 (6)	3.7 (3)
HH	-90.0 to 90.0	6.6	3.5 (53)	1.7 (26)	0.6 (9)	0.3 (4)	0.2 (3)
HH	-25.0 to 25.0	4.4	2.7 (62)	1.2 (26)	0.3 (6)	0.1 (2)	0.0 (1)

our mode-based value. The total semidiurnal energy summed over the first 5 modes (111 PJ) is in agreement with the KE value obtained by Buijsman et al. (2020) (their Figure 9a), after correcting for the contributions of the deep-water barotropic to baroclinic energy conversion of S_2 and N_2 (Egbert and Ray, 2003). The fraction of mode 1 supertidal energy (62%) is the largest equatorward of ±25°. In the equatorial region, the mode 1 supertidal KE comprises about 5% of the semidiurnal KE.

3.4.3. Regional Patterns

To highlight regional differences in modal energy content per frequency, we show KE energy spectra P_{KE} of the modal amplitude time series for four deep-water locations in Figure 10. Offshore of the Amazon shelf in strong supertidal internal tide beams, power spectral density of modes 1 and 2 is characterized by higher harmonics of M_2, with the most energy in M_4 and M_6. The M_4 peak is about one order of magnitude lower than the M_2 peak. The dominance of higher harmonics such as M_4 and M_6 suggests that this supertidal beam is of tidal origin. While supertidal energy in modes 1-2 remains relatively high, modes 3 and higher, quickly roll off with slopes steeper than ω^{-4}. At the other locations, the supertidal tails of mode 1 are also much flatter than for the higher modes. Another site with relatively strong mode-1 supertidal energy is Georges Bank (Figure 10c and also bottom left panel of Figure 7), with distinct M_4 and M_6 peaks. The M_4 peak is about 2 orders of magnitude lower than the M_2 peak. In contrast, to the north of Hawaii, the internal tide is mostly linear and higher harmonics are not well

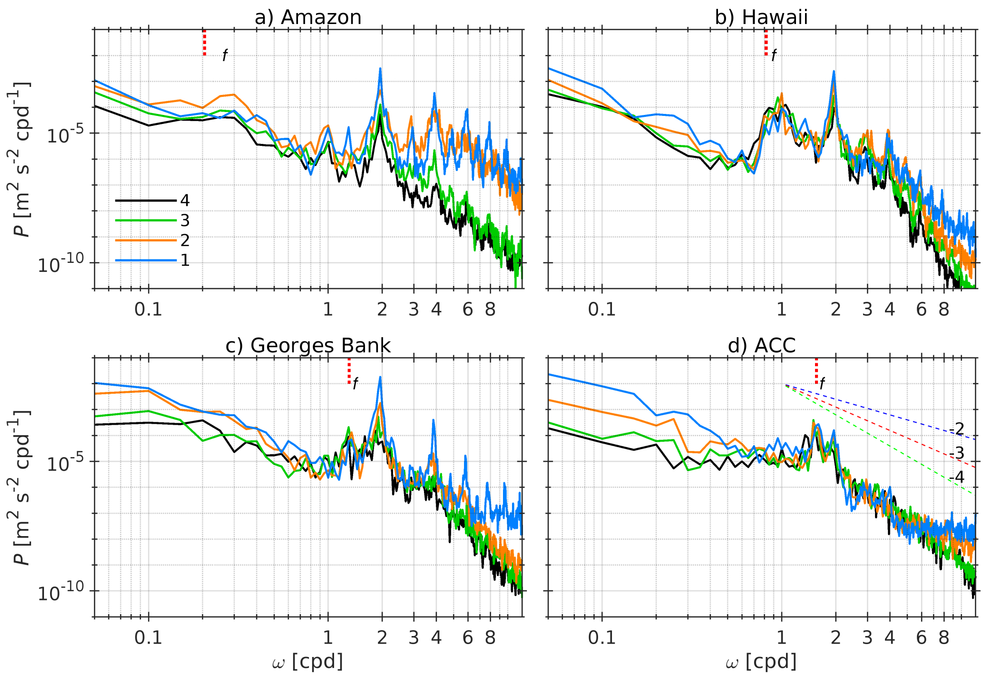

Figure 10: Kinetic energy spectra for modes 1-4 for four deep water sites: (a) near the Amazon shelf (5.87°N, 317.32°E), (b) north of Hawaii (24.06°N, 203.52°E), (c) near Georges Bank (40.74°N, 296.40°E), and (d) in an anticyclonic eddy in the ACC (51.05°S, 146.84°E). The diagonal dashed lines in (d) show ω^{-2}, ω^{-3}, and ω^{-4} and the vertical red dashed line marks the local inertial frequency magnitude.

developed. The mode-1 M_4 peak is about 2.5 orders of magnitude lower than the M_2 peak. To contrast, we also show P_{KE} in an area with strong mesoscale variability and weak internal tides in Figure 10d. This site is located due south of Tasmania. Of the four sites considered, mode-1 subtidal P_{KE} is the largest here. At this site, an anticyclonic eddy traps near-inertial wave modes causing the near-inertial peak to be larger than the semidiurnal tidal peak.

We conclude the Results section with a discussion on the mode-1 and 2 energy flux patterns for the subtidal, semidiurnal, and supertidal bands at Georges Bank (Figure 11) and the Amazon shelf (Figure 12). At Georges Bank, the Gulfstream (GS) meanders interact with an energetic semidiurnal internal tide beam (e.g., Duda et al., 2018). At the location of the Gulfstream meanders, mode 1 and 2 subtidal fluxes in Figure 11a and b are organized in anticyclonic closed loop gyres (clockwise in the Northern Hemisphere), some of them elongated in shape. These flux gyres do not correlate with anticyclonic warm core eddies. For example, a cyclonic cold core eddy at 36.5°N and 298°E supports two anticyclonic flux gyres. The mode 1 subtidal fluxes are better organized and larger ($\mathcal{O}(100)$ kW/m) than the mode 2 fluxes ($\mathcal{O}(10)$ kW/m). The closed-loop appearance suggests that the net energy transport and flux divergence are small. However, further investigations into these gyres are beyond the scope of this paper.

The semidiurnal and supertidal mode 1 and 2 energy fluxes are affected by the GS meanders in various ways in Figure 11c-f. The semidiurnal mode 1 beam that is generated at Georges Bank has a magnitude of about 10 kW/m near the generation site. However, it quickly loses power after crossing the GS front near 40°N, suggesting wave-mean flow energy exchanges and wave scattering due to the mean flow (Dunphy and Lamb, 2014; Kelly and Lermusiaux, 2016). The GS front also seems to reflect some energy (1-2 kW/m) northeastward near 298°E. Only about 1 kW/m of semidiurnal mode 2 flux is generated at the shelf in several narrow beams (Figure 11d). Weaker semidiurnal mode 2 fluxes of $\mathcal{O}(100)$ W/m radiate northward and southward from the front with strong positive vorticity near 40°N and 298°E. It is not clear from this analysis if this energy originates from the eastward refracted semidiurnal mode 2 beam or from semidiurnal mode 1 energy scattering. Supertidal mode 1 energy flux of about 1 kW/m is also generated near the shelf (Figure 11e). Compared to the semidiurnal mode 1, supertidal mode 1 is more affected by reflection and refraction. Albeit smaller than the supertidal mode 1 flux, the supertidal mode 2 flux in Figure 11f is not only generated near the shelf, where the supertidal mode 1 flux is relatively large, but also at the front near 40°N and 298°E, from where it is radiated northward.

Although the fluxes associated with the geostrophic turbulence due to the equatorial currents at the Amazon shelf in Figure 12a and b are substantially weaker than in the Gulfstream, they are still organized in clockwise flux gyres. While the semidiurnal mode 1 and 2 fluxes originate from the shelf in Figure 12c and d due to barotropic to baroclinic conversion, the supertidal fluxes in Figure 12e and f appear in the open ocean, away from topography. In contrast to Georges Bank, the tidal and supertidal fluxes are less affected by the mesoscale currents along the Amazon shelf.

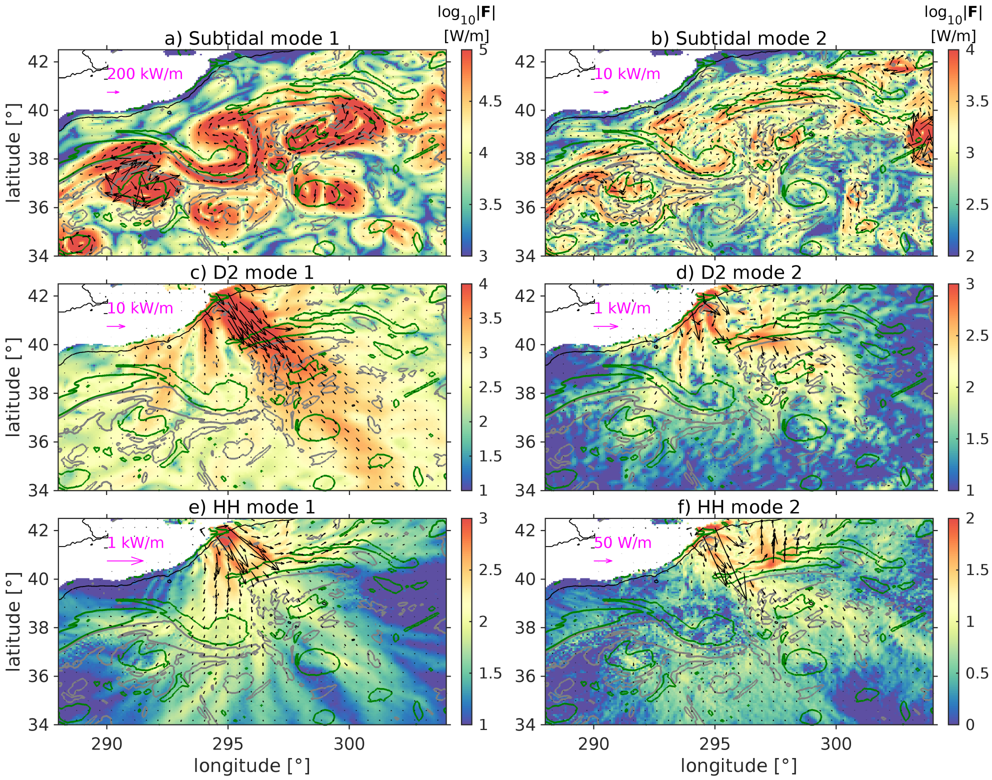

Figure 11: Mode 1 and mode 2 flux magnitudes for the (a,b) subtidal, (c,d) semidiurnal, and (e,f) supertidal bands at Georges Bank at the United States northeast coast. Green (gray) contours indicate positive (negative) time-mean surface relative vorticity $\xi/f = 0.1$ ($\xi/f = -0.1$). The colormaps are scaled differently for each subplot.

4. Discussion

4.1. Validity of the Grid Spacing-Criteria

In this paper we have presented several criteria to determine how many vertical modes are resolved due to the horizontal and vertical grid spacings in a global HYCOM simulation (Table 1). In this section we elaborate on the usefulness of these criteria. For this purpose, we compare the predictions of the zonal-mean number of resolved modes in Figure 4 with the zonal-mean captured velocity ($R^2_{KE,n}$) and pressure ($R^2_{p,n}$) variance in Figure 6.

When the vertical grid-spacing criterion CZ1 is applied to the hybrid vertical coordinate (CZ1-h; Figure 4), it is clearly too strict. It predicts that mode 1 is barely resolved globally, which is certainly not the case when

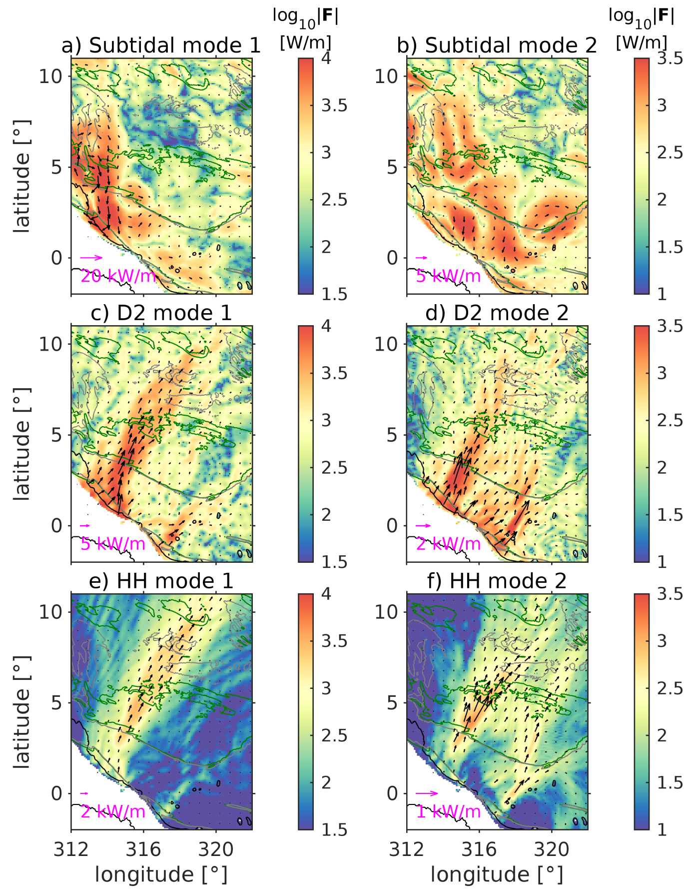

Figure 12: The same as Figure 11, but for the Amazon Shelf.

considering the captured variance across all frequency bands in Figures 5 and 6. The application of CZ1 to the z coordinates (CZ1-z) is merely illustrative because we ignore the isopical layers. Hence, we focus on the applicability of the CZ2 and CZ3 criteria.

Equatorward of $\pm 25°$, substantial subtidal velocity variance is captured by modes 6-10 in Figure 6a, implying that criterion CZ2 is too strict as compared to CZ3 (Figure 4a). Moreover, $R^2_{KE,10}$ has a minimum in the tropics, indicating that more modes could have been resolved (on average 12, according to CZ3 in Figure 4a). Poleward of $\pm 25°$, the high-mode variance is reduced while $R^2_{KE,10}$ increases towards unity. These variance trends at the mid to high latitudes are in agreement with the trends of both the horizontal grid-spacing criterion and CZ3, both of which allow for fewer modes to be resolved in the poleward direction (Figure 4a). For example at $\pm 40°$, the ten resolved modes fall outside the range predicted by the horizontal grid-spacing criterion (6-8, excluding the standard deviation), while they are in agreement with CZ3. In contrast, only 5-6 modes explain the undecomposed pressure variance globally in Figure 6e. While this overlaps with the CZ2 predictions near the equator, CZ2 is too strict at high latitudes.

At the equator, more than ten modes are needed to explain the diurnal velocity variance in Figure 6b, which is more than predicted by CZ2 (on average six) and by the horizontal grid-spacing criterion (maximally 9) in Figure 4b. At this location, CZ3 predicts on average 12 modes, which may be more in agreement with the captured variance. Poleward of $\pm 30°$, the diurnal kinetic energy is small (Figure 9b) and the velocity variance is affected by trapped, near-inertial, and subtidal motions. Equatorward of $\pm 25°$, the captured diurnal variance in the pressure modes is similar to the subtidal variance, with 4-5 modes capturing most of the variance (Figure 6f). However, this is less than predicted by CZ2 (on average six).

The semidiurnal velocity variance in mode 4 is easily captured globally (Figure 6c). However, CZ2 limits the number of modes resolved to < 4 south of 50°S (Figure 4c), suggesting CZ2 may not be the best criterion. At the equator, slightly more variance is captured (up to mode 6) than predicted by the horizontal grid-spacing criterion (up to mode 5) in Figure 4c. However, the poleward increase in the number of modes resolved due to the horizontal grid-spacing criterion (Figure 4) agrees with the decrease in the captured variance by modes 1-5 and the increase in the captured variance by modes 6-10 (Figure 6c). At $\pm 50°$, the line for the horizontal grid-spacing criterion intersects CZ3 at 7-8 modes in Figure 4c, which is similar to the number of modes that explain the velocity variance in Figure 6c at these latitudes. To the south of 50°S the captured low-mode variance increases while the high-mode variance decreases in Figure 6c in agreement with the decrease in the number of modes resolved due to the vertical grid-spacing criterion CZ3. For the pressure modes, most of the variance is explained by modes 1-4 globally without clear meridional trends (Figure 6g). This number is in accordance with the horizontal grid-spacing criterion at the equator but more than CZ2 predicts poleward of 60°S.

Most of the supertidal velocity variance equatorward of $\pm 25°$ is captured by the first four supertidal modes, while at higher latitudes some variance is also captured by higher modes (Figure 6d). Equatorward of $\pm 25°$ this variance is mostly of tidal origin, whereas poleward of $\pm 25°$ the higher mode variance may also result from mesoscale and near-inertial motions. Although the horizonal grid-spacing criterion in Figure 4d generally under predicts the number of velocity modes resolved by 1-2, the poleward increase in the higher-mode variance agrees somewhat with the slight meridional trend of the horizonal grid-spacing criterion. In contrast, the pressure-mode variance in Figure 6h is explained by three modes globally, which is in closer agreement to the horizonal grid-spacing criterion in Figure 4d.

The picture that emerges from the above discussion is that 1) the meridional trends in captured velocity variance agree best with the trends in the number of resolved modes due to the combination of the horizontal grid-spacing criteria for the different frequency bands and the vertical grid-spacing criterion CZ3 and 2) CZ2 is irrelevant. Moreover, the number of captured modes is larger than the upper limit predicted by the horizontal grid-spacing criteria, which is determined by $\gamma = 6$ cells/wavelength. In addition to predicting the resolution of low-mode propagating waves with both pressure and velocity variance (waves with a pressure flux; Figure 8), we hypothesize that CZ3 also predicts the additional resolution of high-mode "noise" or standing waves with large velocity and little pressure variance (e.g., near-inertial waves). For subtidal and diurnal velocity modes, CZ3 appears to be a better predictor than the stricter horizontal grid-spacing criterion, which is not very useful for modes that do not propagate.

In contrast, the pressure variance is captured by fewer modes than the velocity variance and its trends only weakly reflect the trends in the horizontal grid-spacing and CZ2. The only clear trend captured by the pressure modes is that more variance is captured by the higher modes corresponding to an increase in wavelength from supertidal to semidiurnal to diurnal frequencies. We hypothesize that the pressure mode variance reflects the propagating waves, which require a stricter vertical grid-spacing criterion than ZC3 (but not ZC2) for the subtidal and diurnal modes and which are reasonably well predicted by the horizontal resolution criterion for semidiurnal and supertidal modes.

We would like to emphasize that our criteria are approximations and they should not be interpreted as firm cutoffs beyond which modes are no longer resolved. Variance may also project on modes with wavelengths that are resolved by fewer grid cells than what is used in our criteria. It is likely that these modes will decay more quickly as compared to a simulation in which they are fully resolved.

4.2. Supertidal Modes

Our HYCOM simulation resolves the first two supertidal modes with kinetic energy and fluxes that are largest at low latitudes (Figures 7, 8, and 9d). The energy spectra in Figure 10 indicate that the supertidal energy is mostly concentrated in the higher harmonics of the M_2 tide (M_4, M_6, etc), reflecting the tidal origin of these modes. Higher harmonic motions have also been observed and simulated in the open ocean in agreement with our simulation. For example, the strong M_2 internal tide generation in the Bay of Biscay also coincides with observations (van Haren et al., 2002; van Aken et al., 2007; van Haren and Maas, 2022) and model simulations (Pichon et al., 2013) of deep open ocean currents that have energy at the higher harmonic frequencies of M_2. Similarly, higher harmonics are also simulated offshore the Amazon shelf (Tchilibou et al., 2022). Global drifter observations (Yu et al., 2019) and model simulations (Arbic et al., 2022) of near-surface kinetic energy also reveal these tidal higher harmonics are ubiquitous.

These supertidal modes mostly occur at strong semidiurnal internal tide generation sites at low latitudes, such as the Andaman and Nicobar Islands in the Bay of Bengal, Luzon Strait, the central Pacific including the French Polynesian Islands, Amazon Shelf, and the Mascarene Ridge. As these strong semidiurnal internal tides propagate away from their generation sites, they steepen and cascade energy to shorter wavelengths and supertidal frequencies (i.e., solitons) via superharmonic wave-wave interactions (e.g., Sutherland and Dhaliwal, 2022). These wave-wave interactions are enhanced in areas where the stratification is strong (see Figure 1) and the background rotation is weak (Sutherland and Dhaliwal, 2022). This nonlinear energy transfer mostly occurs in the open ocean away from topography. This is evident for the beam at the Amazon shelf in Figure 12e and f and to the north of the French Polynesian Islands (0°N and 220°E; Figure 8), where the supertidal mode 1 energy flux peaks at the equator. In a companion study of the same HYCOM simulation used in this paper, Solano et al. (under review) has quantified the energy transfers from the tidal to the supertidal band and has correlated the location of these supertidal beams with the occurrence of solitary wave surface signatures in satellite imagery (Jackson, 2007).

An interesting feature of the supertidal energy fluxes in Figure 8 is that the beams are well defined and that they extend across the tropics for 1000s of km. For example, the Amazon beams extend to the Iberian Peninsula and northwest Africa. Similarly, the French Polynesian Island beams reach the Bahia Peninsula in North America. The semidiurnal mode 1 beams from the respective generation sites in Figure 8 do not appear to extend that far, most likely because they disappear in the mode 1 background noise. We hypothesize that the model resolution is not sufficient to cascade this supertidal energy to higher frequencies and wavenumbers and that the vertical shear in these low modes is too weak to trigger dissipation due to the KPP subgrid scale mixing scheme. Hence, the decay is small and energy is stuck in these low supertidal modes. A future objective is to compare the supertidal signal in the HYCOM simulations with in-situ observations, i.e., moorings and/or satellite altimetry.

5. Conclusions

In this study, we have computed the captured variance and energy terms across subtidal, diurnal, semidiurnal, and supertidal frequency bands for the first ten vertical modes in a 30-day global HYCOM simulation that is forced with tides and atmospheric fields. We have estimated the number of modes that are resolved globally in the simulation due to the horizontal and vertical grid spacings, and have validated these predictions with the captured variance and energetics. Our key findings are as follows:

- A new result is the projection of vertical modes on the subtidal circulation in a global model simulation. Subtidal modes have most of their kinetic energy in mode 1 (60% of the energy summed over modes 1-10). Their energy density is largest in the ACC and western boundary currents. The global subtidal kinetic energy content in modes 1-10 is about 740 PJ, which is about six times larger than the energy content in the semidiurnal modes.

- The diurnal kinetic energy is strongest equatorward of $\pm 30°$, mostly due to the diurnal internal tide generation in the western Pacific Ocean. Near the turning latitudes, diurnal energy also projects on higher modes due to near-inertial waves.

- For the semidiurnal modes, about 50% of the kinetic energy summed over the first ten modes is contained in mode 1, with a gradual decrease in energy content for the higher modes.

- We also report for the first time on the modal kinetic energy and energy fluxes in the supertidal band (> 2.15 cpd) in global simulations. The supertidal kinetic energy and flux are mostly captured by the first two modes and strongest in the tropics. Here low-mode semidurnal internal tides scatter energy to supertidal modes due to superharmonic wave-wave interactions.

- More variance is captured for higher velocity modes than for higher pressure modes across all frequency bands. We hypothesize that "noise" and non-propagating features, such as high-mode near-inertial waves, project more on velocity modes than on pressure modes. The variance of pressure modes is a better representation of the propagating waves. This difference affects the interpretation of the skill of the horizontal and vertical grid-spacing criteria.

- The meridional trends in the captured velocity variance agree best with the meridional trends in the resolved modes due the horizontal grid-spacing criterion and the vertical grid-spacing criterion CZ3 across all frequency bands. In the former, a vertical mode is not well resolved if less than 6-8 cells occur per horizontal wavelength, and in the latter, if pairs of subsequent horizontal or vertical velocity eigenfunction zero-crossings occur in the same isopycnal layer.

- In agreement with the captured variance, the horizontal grid-spacing criterion is stricter than the vertical grid-spacing criterion in predicting the number of resolved semidiurnal modes at low to mid latitudes and supertidal modes globally.

- The application of the vertical grid-spacing criterion to z-coordinate models ($\sim$6 vertical layers/wavelength based on Stewart et al., 2017) is not suitable for isopycnal layer models. It predicts that only 0-1 modes are resolved in our simulations, whereas we compute substantial variance in higher modes in most frequency bands.

Acknowledgments

M. Buijsman and M. Solano are funded by the Office of Naval Research (ONR) grant N000141912704. M. Buijsman is also funded by National Aeronautic Space Administration (NASA) grants 80NSSC18K0771 and NNX17AH55G. J. Shriver acknowledges support from ONR grant N0001423WX01413. B.K.

Arbic acknowledges support from ONR grant N00014-19-1-2712. E.P. Chassignet, L. Hiron, and X. Xu acknowledge support from ONR grants N00014-19-1-2717 and N00014-20-1-2769 and from NASA grant 80NSSC20K1135. We thank Gregg Jacobs of the Naval Research Laboratory for feedback on finite difference amplitude errors.

Data Availability Statement

The raw HYCOM simulation data of ∼40 terabytes (TB) and diagnosed fields are available upon request for those that have access to the United States Department of Defense super computers. The seafloor depth, grid coordinates, eigenspeeds for modes 1-5, and the time-mean kinetic energy and energy fluxes for modes 1-5 for four frequency bands are accessible at Zenodo: https://doi.org/10.5281/zenodo.7909290.

Appendix A. Amplitude Error due to Finite Differences

To better understand how the horizontal grid spacing affects the number of resolved wave modes, we consider how finite difference errors of a sinusoidal wave change with respect to horizontal grid spacing. It is likely that errors are further increased when considering time integration and advective terms. Hence, the following analysis is an estimate of the minimum error.

Given a grid of spacing Δx, noting the position at the k^{th} point $x_k = k\Delta x$ and the value of a function at the point $f(x_k) = f_k$, we define the second order centered finite difference of a first derivative as

$$\left.\frac{df}{dx}\right|_{x_k} = \frac{f_{k+1} - f_{k-1}}{2\Delta x} + \epsilon_k, \tag{A.1}$$

where ϵ_k is the error involved in the finite difference estimate. Assume the function is only a sinusoid: $f(x_k) = e^{i(\lambda x_k + \phi)}$, where λ is the wavenumber measured in units of radians per unit of x, and ϕ is a phase offset measured in radians. Then the derivative is

$$\left.\frac{df}{dx}\right|_{x_k} = \frac{e^{i(\lambda(k+1)\Delta x+\phi)} - e^{i(\lambda(k-1)\Delta x+\phi)}}{2\Delta x} + \epsilon_k, \tag{A.2}$$

and the error is

$$\epsilon_k = \frac{e^{i(\lambda(k+1)\Delta x+\phi)} - e^{i(\lambda(k-1)\Delta x+\phi)}}{2\Delta x} - i\lambda e^{i(\lambda k\Delta x+\phi)}. \tag{A.3}$$

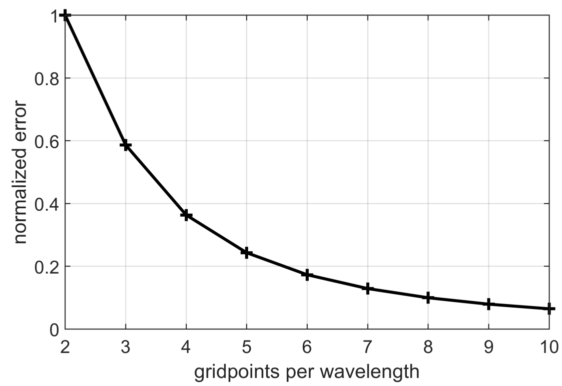

Figure A.13: Amplitude error as a function of the number of gridcells per wavelength normalized by the amplitude of $d(\sin(\lambda x))/dx$.

After some algebra, we find

$$\begin{aligned}\epsilon_k &= \frac{e^{i\lambda k\Delta x}(e^{i\lambda\Delta x} - e^{-i\lambda\Delta x})e^{i\phi}}{2\Delta x} - i\lambda e^{i\lambda k\Delta x}e^{i\phi} \\ &= e^{i\lambda k\Delta x}e^{i\phi}\left(\frac{e^{i\lambda\Delta x} - e^{-i\lambda\Delta x}}{2\Delta x} - i\lambda\right).\end{aligned} \tag{A.4}$$

The amplitude of the error A_{ϵ_k} is a product of three terms, the first two of which are 1. Therefore,

$$\begin{aligned}A_{\epsilon_k} &= \left|\frac{e^{i\lambda\Delta x} - e^{-i\lambda\Delta x}}{2\Delta x} - i\lambda\right| \\ &= \left|\frac{\sin(\lambda\Delta x)}{\Delta x} - \lambda\right|.\end{aligned} \tag{A.5}$$

In Figure A.13, the amplitude of the error, normalized by the amplitude of the slope function $d(\sin(\lambda x + \phi))/dx$ is plotted vs. the number of grid points per wavelength $\frac{2\pi}{\lambda\Delta x}$. In the limit of $\Delta x \to 0$, the amplitude of the error $A_{\epsilon_k} \to 0$. The normalized amplitude error A_{ϵ_k}/λ is about 10% for eight grid cells in a wavelength (Figure A.13).

References

Althaus, A.M., Kunze, E., Sanford, T.B., 2003. Internal tide radiation from mendocino escarpment. Journal of Physical Oceanogry 33, 1510–1527.

Ansong, J.K., Arbic, B.K., Simmons, H.L., Alford, M.H., Buijsman, M.C., Timko, P.G., Richman, J.G., Shriver, J.F., Wallcraft, A.J., 2018. Geographical distribution of diurnal and semidiurnal parametric subharmonic instability in a global ocean circulation model. Journal of Physical Oceanography 48, 1409–1431.

Arbic, B., Alford, M., Ansong, J., Buijsman, M., Ciotti, R., Farrar, J., Hallberg, R., Henze, C., Hill, C., Luecke, C., D.Menemenlis, E.J.Metzger, Müller, M., Nelson, A., Nelson, B., Ngodock, H., Ponte, R., Richman, J., Savage, A., Scott, R., Shriver, J., Simmons, H., Souopgui, I., Timko, P., Wallcraft, A., Zamudio, L., Zhao, Z., 2018. A primer on global internal tide and internal gravity wave continuum modeling in HYCOM and MITgcm, in: Chassignet, E., Pascual, A., Tintore, J., Verron, J. (Eds.), New frontiers in operational oceanography. GODAE OceanView, pp. 307–392. doi:10.17125/gov2018.ch13.

Arbic, B.K., 2022. Incorporating tides and internal gravity waves within global ocean general circulation models: A review. Progress in Oceanography 206, 102824. doi:10.1016/j.pocean.2022.102824.

Arbic, B.K., Elipot, S., Brasch, J.M., Menemenlis, D., Ponte, A.L., Shriver, J.F., Yu, X., Zaron, E.D., Alford, M.H., Buijsman, M.C., Abernathey, R., Garcia, D., Guan, L., Martin, P.E., Nelson, A.D., 2022. Near-surface oceanic kinetic energy distributions from drifter observations and numerical models. Journal of Geophysical Research: Oceans 127, e2022JC018551. doi:10.1029/2022JC018551.

Arbic, B.K., Garner, S.T., Hallberg, R.W., Simmons, H.L., 2004. The accuracy of surface elevations in forward global barotropic and baroclinic tide models. Deep-Sea Research II 51, 3069–3101.

Bleck, R., 2002. An oceanic general circulation model framed in hybrid isopycnic cartesian coordinates. Ocean Modelling 4, 55–88.

Buijsman, M., Ansong, J., Arbic, B., Richman, J., Shriver, J., Timko, P., Wallcraft, A., Whalen, C., Zhao, Z., 2016. Impact of parameterized internal wave drag on the semidiurnal energy balance in a global ocean circulation model. Journal of Physical Oceanogry 46, 1399–1419. doi:10.1175/JPO-D-15-0074.1.

Buijsman, M.C., Kanarska, Y., McWilliams, J.C., 2010. On the generation and evolution of nonlinear internal waves in the South China Sea. Journal of Geophysical Research 115. doi:10.1029/2009JC005275.

Buijsman, M.C., Stephenson, G.R., Ansong, J.K., Arbic, B., Green, M., Shriver, J.G.R.J., Vic, C., Wallcraft, A., Zhao, Z., 2020. On the interplay between horizontal resolution and wave drag and their effect on tidal baroclinic mode waves in realistic global ocean simulations. Ocean Modelling 152. doi:10.1016/j.ocemod.2020.101656.

Carton, J.A., Giese, B.S., 2008. A reanalysis of ocean climate using simple ocean data assimilation (SODA). Monthly Weather Review 136, 2999–3017.

Chassignet, E., Hurlburt, H., Metzger, E., Smedstad, O., Cummings, J., Halliwell, G., Bleck, R., Baraille, R., Wallcraft, A., Lozano, C., Tolman, H., Srinivasan, A., Hankin, S., Cornillon, P., Weisberg, R., Barth, A., He, R., Werner, F., Wilkin, J., 2009. U.s. godae: Global ocean prediction with the HYbrid Coordinate Ocean Model (HYCOM). Oceanography 22, 64–75.

Chassignet, E., Smith, L., Halliwell, G., Bleck, R., 2003. North Atlantic simulations with the HYbrid Coordinate Ocean Model (HYCOM): Impact of the vertical coordinate choice, reference density, and thermobaricity. Journal of Physical Oceanography 33, 2504–2526.

Chelton, D.B., deSzoeke, R.A., Schlax, M.G., Naggar, K.E., Siwertz, N., 1998. Geographical variability of the first baroclinic rossby radius of deformation. Journal of Physical Oceanography 28, 433–460. doi:10.1175/1520-0485(1998)028$<$0433:GVOTFB$>$2.0.CO;2.

Chelton, D.B., Schlax, M.G., Samelson, R.M., 2011. Global observations of nonlinear mesoscale eddies. Progress in Oceanography 91. doi:10.1016/j.pocean.2011.01.002.

Duda, T., Lin, Y., Buijsman, M., Newhall, A., 2018. Internal tidal modal ray refraction and energy ducting in baroclinic gulf stream currents. Journal of Physical Oceanography 48, 1969–1993. doi:10.1175/JPO-D-18-0031.1.

Dunphy, M., Lamb, K.G., 2014. Focusing and vertical mode scattering of the first mode internal tide by mesoscale eddy interaction. Journal of Geophysical Research 119, 523–536.

Egbert, G.D., Erofeeva, S.Y., 2021. An approach to empirical mapping of incoherent internal tides with altimetry data. Geophysical Research Letters 48, e2021GL095863. doi:10.1029/2021GL095863.

Egbert, G.D., Ray, R.D., 2003. Semi-diurnal and diurnal tidal dissipation from TOPEX/Poseidon altimetry. Geophysical Research Letters 30. doi:10.1029/2003GL017676.

Emery, W.J., Thomson, R.E., 2001. Data Analysis Methods in Physical Oceanography (Second and Revised Edition). Elsevier, Amsterdam.

Ferrari, R., Wunsch, C., 2010. The distribution of eddy kinetic and potential energies in the global ocean. Tellus A 62, 92–108. doi:10.1111/j.1600-0870.2009.00432.x.

Fu, L.L., Alsdorf, D., Rodriguez, E., Morrow, R., Mognard, N., Lambin, J., Vaze, P., , Lafon, T., 2010. The swot (surface water and ocean topography) mission: Spaceborne radar interferometry for oceanographic and hydrological applications, in: Hall, J., Harrison, D., Stammer, D. (Eds.), Proceedings of OceanObs'09: Sustained Ocean Observations and Information for Society (Vol. 2), Venice, Italy, 21-25 September 2009, ESA Publication WPP-306. URL: https://swot.jpl.nasa.gov/system/publications/23_23_oceanobs09_swot.pdf, doi:10.5270/OceanObs09.cwp.33.

Geoffroy, G., Nycander, J., Buijsman, M.C., Shriver, J.F., Arbic, B.K., 2022. Validating the spatial variability of the semidiurnal internal tide in a realistic global ocean simulation with argo and mooring data. EGUsphere [preprint] URL: 10.5194/egusphere-2022-1085.

Gill, A.E., 1982. Atmosphere-ocean dynamics. Academic Press.

Gong, Y., Rayson, M.D., Jones, N.L., Ivey, G.N., 2021. Directional decomposition of internal tides propagating from multiple generation sites. Ocean Modelling 162. doi:10.1016/j.ocemod.2021.101801.

Hallberg, R., 2013. Using a resolution function to regulate parameterizations of oceanic mesoscale eddy effects. Ocean Modelling 72, 92–103. doi:10.1016/j.ocemod.2013.08.007.

Hazewinkel, J., Winters, K., 2011. Psi of the internal tide on a β plane: flux divergence and near-inertial wave propagation. Journal of Physical Oceanography 41, 1673–1682.

Huang, R., 2010. Ocean circulation, wind-driven and thermohaline processes. Cambridge University Press.

Jackson, C., 2007. Internal wave detection using the moderate resolution imaging spectroradiometer (modis). Journal of Geophysical Research: Oceans 112. doi:10.1029/2007JC004220.

Kelly, S.M., 2016. The vertical mode decomposition of surface and internal tides in the presence of a free surface and arbitrary topography. Journal of Physical Oceanography 46, 3777–3788. doi:10.1175/JPO-D-16-0131.1.

Kelly, S.M., Lermusiaux, P.F., 2016. Internal-tide interactions with the gulf stream and middle atlantic bight shelfbreak front. Journal of Geophysical Research: Oceans 121. doi:10.1002/2016JC011639.

Kelly, S.M., Nash, J.D., Martini, K.I., Alford, M.H., Kunze, E., 2012. The cascade of tidal energy from low to high modes on a continental slope. Journal of physical oceanography 42, 1217–1232.

Kelly, S.M., Waterhouse, A.F., Savage, A.C., 2021. Global dynamics of the stationary m2 mode-1 internal tide. Geophysical Research Letters 48. doi:10.1029/2020GL091692.

Li, Z., von Storch, J.S., 2020. M2 internal-tide generation in stormtide2. Journal of Geophysical Research: Oceans 125, e2019JC015453. doi:10.1029/2019JC015453.

Mak, J., Avdis, A., David, T., Lee, H.S., Na, Y., Wang, Y., Yan, F.E., 2022. On constraining the mesoscale eddy energy dissipation time-scale. Journal of Advances in Modeling Earth Systems 14, e2022MS003223. doi:10.1029/2022MS003223.

Morrow, R., Fu, L.L., Ardhuin, F., Benkiran, M., Chapron, B., Cosme, E., d'Ovidio, F., Farrar, J.T., Gille, S.T., Lapeyre, G., Le Traon, P.Y., Pascual, A., Ponte, A., Qiu, B., Rascle, N., Ubelmann, C., Wang, J., Zaron, E.D., 2019. Global observations of fine-scale ocean surface topography with the surface water and ocean topography (swot) mission. Frontiers in Marine Science 6. doi:10.3389/fmars.2019.00232.

Müller, M., Arbic, B., Richman, J., Shriver, J., Kunze, E., Scott, R.B., Wallcraft, A., Zamudio, L., 2015. Toward an internal gravity wave spectrum in global ocean models. Geophysical Research Letters 42, 3474–3481. doi:10.1002/2015GL063365.

Muller, M., Cherniawsky, J., Foreman, M., von Storch, J., 2012. Global m2 internal tide and its seasonal variability from high resolution ocean circulation and tide modeling. Geophysical Research Letters 39, L19607.

Ngodock, H.E., Souopgui, I., Wallcraft, A.J., Richman, J.G., Shriver, J.F., Arbic, B.K., 2016. On improving the accuracy of the m_2 barotropic tides embedded in a high-resolution global ocean circulation model. Ocean Modelling 97, 16–26. doi:10.1016/j.ocemod.2015.10.011.

Pan, Y., Haley, P.J., Lermusiaux, P.F., 2021. Interactions of internal tides with a heterogeneous and rotational ocean. Journal of Fluid Mechanics 920, A18. doi:10.1017/jfm.2021.423.

Pichon, A., Morel, Y., Baraille, R., Quaresma, L.S., 2013. Internal tide interactions in the bay of biscay: Observations and modelling. Journal of Marine Systems 109–110, S26–S44. doi:10.1016/j.jmarsys.2011.07.003.

Raja, K.J., Buijsman, M.C., Shriver, J.F., Arbic, B.K., Siyanbola", O., 2022. Near-inertial wave energetics modulated by background flows in a global model simulation. Journal of physical oceanography 52, 823–840. doi:10.1175/JPO-D-21-0130.1.

Rocha, C.B., Gille, S.T., Chereskin, T.K., Menemenlis, D., 2016. Seasonality of submesoscale dynamics in the kuroshio extension. Geophysical Research Letters 43, 11304–11311. doi:https://doi.org/10.1002/2016GL071349.

Savage, A.C., Arbic, B.K., Alford, M.H., Ansong, J.K., Farrar, J.T., Menemenlis, D., O'Rourke, A.K., Richman, J.G., Shriver, J.F., Voet, G., Wallcraft, A.J., Zamudio, L., 2017. Spectral decomposition of internal gravity wave sea surface height in global models. Journal of Geophysical Research: Oceans 122, 7803–7821. doi:10.1002/2017JC013009.

Shriver, J.F., Arbic, B.K., Richman, J.G., Ray, R.D., Metzger, E.J., Wallcraft, A.J., Timko, P.G., 2012. An evaluation of the barotropic and internal tides in a high resolution global ocean circulation model. Journal of Geophysical Research: Oceans 117. doi:10.1029/2012JC008170.

Simmons, H.L., Alford, M.H., 2012. Simulating the long-range swell of internal waves generated by ocean storms. Oceanography 25, 30–41. URL: https://doi.org/10.5670/oceanog.2012.39.

Simmons, H.L., Hallberg, R.W., Arbic, B.K., 2004. Internal wave generation in a global baroclinic tide model. Deep-Sea Research II 51, 3043–3068.

Siyanbola, O.Q., Buijsman, M.C., Delpech, A., Renault, L., Barkan, R., Shriver, J.F., Arbic, B.K., McWilliams, J.C., 2023. Remote internal wave forcing of regional ocean simulations near the u.s. west coast. Ocean Modelling 181, 102154. doi:10.1016/j.ocemod.2022.102154.

Solano, M., Buijsman, M.C., Shriver, J., Magalhaes, J., da Silva, J.C.B., Jackson, C., Arbic, B., Barkan, R., under review. Nonlinear internal tides in a realistically forced global ocean simulation. Journal of Geophysical Research .

Stewart, K.D., Hogg, A.M.C., Griffies, S.M., Heerdegen, A.P., Ward, M.L., Spence, P., England, M.H., 2017. Vertical resolution of baroclinic modes in global ocean models. Ocean Modelling 113, 50–65. doi:10.1016/j.ocemod.2017.03.012.

Sutherland, B.R., Dhaliwal, M.S., 2022. The nonlinear evolution of internal tides. part 1: the superharmonic cascade. Journal of Fluid Mechanics 948, A21. doi:10.1017/jfm.2022.689.

Tchilibou, M., Koch-Larrouy, A., Barbot, S., Lyard, F., Morel, Y., Jouanno, J., Morrow, R., 2022. Internal tides off the amazon shelf during two contrasted seasons : Interactions with background circulation and ssh imprints. Ocean Science Discussions doi:10.5194/os-2021-114.

Tedesco, P., Gula, J., Penven, P., Ménesguen, C., 2022. Mesoscale eddy kinetic energy budgets and transfers between vertical modes in the agulhas current. Journal of Physical Oceanography 52, 677–704. doi:10.1175/JPO-D-21-0110.1.

van Aken, H.M., van Haren, H., Maas, L.R.M., 2007. The high-resolution vertical structure of internal tides and near-inertial waves measured with an adcp over the continental slope in the bay of biscay. Deep-Sea Research Part I: Oceanographic Research Papers 54, 533–556. doi:10.1016/j.dsr.2007.01.003.

van Haren, H., Maas, L., 2022. A simple model for an internal wave spectrum dominated by non-linear interactions. doi:10.48550/ARXIV.2203.00475.

van Haren, H., Maas, L., van Aken, H., 2002. On the nature of internal wave spectra near a continental slope. Geophysical Research Letters 29. doi:10.1029/2001gl014341.

Waterhouse, A.F., MacKinnon, J.A., Nash, J.D., Alford, M.H., Kunze, E., Simmons, H.L., Polzin, K.L., Laurent, L.C.S., Sun, O.M., Pinkel, R., Talley, L.D., Whalen, C.B., Huussen, T.N., Carter, G.S., Fer, I., Waterman, S., Garabato, A.C.N., Sanford, T.B., Lee, C.M., 2014. Global patterns of diapycnal mixing from measurements of the turbulent dissipation rate. Journal of Physical Oceanography 44, 1854–1872.

Wunsch, C., 1997. The vertical partition of oceanic horizontal kinetic energy. Journal of Physical Oceanography 27, 1770–1794. doi:https://doi.org/10.1175/1520-0485(1997)027<1770:TVPOOH>2.0.CO;2.

Xu, C., Shang, X., Huang, R., 2011. Estimate of eddy energy generation/dissipation rate in the world ocean from altimetry data. Ocean Dynamics 61, 525–541. doi:10.1007/s10236-011-0377-8.

Xu, X., Chassignet, E.P., Wallcraft, A., 2023. Impact of vertical resolution on representing baroclinic modes and water mass distribution in the north atlantic circulation. submitted to Ocean Modelling .

Xu, X., Chassignet, E.P., Wallcraft, A.J., Arbic, B.K., Buijsman, M.C., Solano, M., 2022. On the spatial variability of the mesoscale sea surface height wavenumber spectra in the atlantic ocean. Journal of Geophysical Research: Oceans 127, e2022JC018769. doi:10.1029/2022JC018769.

Yu, X., Ponte, A.L., Elipot, S., Menemenlis, D., Zaron, E.D., Abernathey, R., 2019. Surface kinetic energy distributions in the global oceans from a high-resolution numerical model and surface drifter observations. Geophysical Research Letters 46, 9757–9766. doi:10.1029/2019GL083074.

Zhao, Z., Alford, M., Girton, J., Rainville, L., Simmons, H., 2016. Global observations of open-ocean mode-1 M_2 internal tides. Journal of Physical Oceanography 46, 1657–1684.

Zilberman, N.V., Becker, J.M., Merrifield, M.A., Carter, G.S., 2009. Model estimates of M_2 internal tide generation over Mid-Atlantic Ridge topography. Journal of Physical Oceanography 39, 2635–2651.